Inorg. Chem. **2007**, *46*, 1741–1750

Steps along the Path to Dihydrogen Activation at [FeFe] Hydrogenase Structural Models: Dependence of the Core Geometry on Electrocatalytic Proton Reduction

Mun Hon Cheah, Stacey J. Borg, and Stephen P. Best*

School of Chemistry, University of Melbourne, Victoria, Australia 3010

Received December 7, 2006

Differences in the rate of electrocatalytic proton reduction by $Fe_2(\mu\text{-}PPh_2)_2(CO)_6$, **DP**, and the linked phosphido-bridged analogue $Fe_2(\mu,\mu\text{-}PPh(CH_2)_3PPh)(CO)_6$, **3P**, suggest that dihydrogen elimination proceeds through a bridging hydride. The reaction path was examined using electrochemical, spectroscopic, and in silico studies where reduction of **3P** gives a moderately stable monoanion [K_{disp}(**3P**$^-$) = 13] and a distorted dianion. The monomeric formulation of **3P**$^-$ is supported by the form of the IR and EPR spectra. EXAFS analysis of solutions of **3P**, **3P**$^-$, and **3P**$^{2-}$ indicates a large increase in the Fe–Fe separation following reduction (from 2.63 to ca. 3.1–3.55 Å). DFT calculations of the **3P**, **3P**$^-$, **3P**$^{2-}$ redox series satisfactorily reproduce the IR spectra in the ν(CO) region and the crystallographic (**3P**) and EXAFS-derived Fe–Fe distances. Digital simulation of the electrocatalytic response for proton reduction indicates a low rate of dihydrogen evolution from the two-electron, two-proton product of **3P** (H_2**3P**), with more rapid dihydrogen evolution following further reduction of H_2**3P**. Because dihydrogen evolution is not observed upon formation of H_2**DP**, dihydrogen evolution at the two-electron-reduced level does not involve protonation of a hydridic Fe–H ligand. The rates of dihydrogen elimination from H_2**DP**, H_2**3P**, and $H_2Fe_2(\mu,\mu\text{-}S(CH_2)_3S)(CO)_6$ (H_2**3S**) are related to the DFT-calculated H–H distances [H_2**3S** (1.880 Å) < H_2**3P** (2.064 Å) < H_2**DP** (3.100 Å)], and this suggests a common reaction path for the thiolato- and phosphido-bridged diiron carbonyl compounds.

Introduction

Together with the task of providing a conceptual framework for understanding biological hydrogen activation, the imperative of a shift to more sustainable technologies—possibly with extensive use of dihydrogen as an energy vector—has stimulated investigations into the chemistry of bridged diiron compounds that are related to the 2Fe3S fragment of the [FeFe] hydrogenase active site.[1] This activity has been sustained, at least in part, by the observation that, in addition to their structural and compositional relationships, the compounds are also functional models of the enzyme, catalyzing H_2/D_2 scrambling[2,3] and proton reduction.[4,5] Although the diiron model compounds present problems associated with overpotential, dioxygen sensitivity, and poorly defined dihydrogen oxidation, the high efficiency of the biological system provides inspiration for the development of biomimetic chemistry that will translate into technologies that will be of practical use. Moreover, the availability of good structural and functional models[6] of the catalytic center of the enzyme presents the opportunity to develop a thorough understanding of the chemistry of the

* To whom correspondence should be addressed. Phone: -61-3-83446505. Fax: -61-3-93475180. E-mail: spbest@unimelb.edu.au.

(1) Nicolet, Y.; Piras, C.; Legrand, P.; Hatchikian, C. E.; Fontecilla-Camps, J. C. *Structure* **1999**, *7*, 13−23. Peters, J. W.; Lanzilotta, W. N.; Lemon, B. J.; Seefeldt, L. C. *Science* **1998**, *282*, 1853−1858.

(2) Zhao, X.; Georgakaki, I. P.; Miller, M. L.; Mejia-Rodriguez, R.; Chiang, C.-Y.; Darensbourg, M. Y. *Inorg. Chem.* **2002**, *41*, 3917−3928.

(3) Tye, J. W.; Hall, M. B.; Georgakaki, I. P.; Darensbourg, M. Y. *Adv. Inorg. Chem.* **2004**, *56*, 1−26.

(4) Gloaguen, F.; Lawrence, J. D.; Rauchfuss, T. B. *J. Am. Chem. Soc.* **2001**, 123, 9476−9477. Capon, J.-F.; Gloaguen, F.; Schollhammer, P.; Talarmin, J. *Coord. Chem. Rev.* **2005**, *249*, 1664−1676. Chong, D.; Georgakaki, I. P.; Mejia-Rodriguez, R.; Sanabria-Chinchilla, J.; Soriaga, M. P.; Darensbourg, M. Y. *J. Chem. Soc., Dalton Trans.* **2003**, 4158−4163. Ott, S.; Kritikos, M.; Åkermark, B.; Sun, L.; Lomoth, R. *Angew. Chem., Int. Ed.* **2004**, *43*, 1006−1009.

(5) Borg, S. J.; Behrsing, T.; Best, S. P.; Razavet, M.; Liu, X.; Pickett, C. J. *J. Am. Chem. Soc.* **2004**, *126*, 16988−16999.

(6) Liu, X.; Ibrahim, S. K.; Tard, C.; Pickett, C. J. *Coord. Chem. Rev.* **2005**, 249, 1641−1652. Tard, C.; Liu, X.; Ibrahim Saad, K.; Bruschi, M.; De Gioia, L.; Davies, S. C.; Yang, X.; Wang, L.-S.; Sawers, G.; Pickett, C. J. *Nature* **2005**, 433, 610−613. Rauchfuss, T. B. *Inorg. Chem.* **2004**, *43*, 14−26. Georgakaki, I. P.; Thomson, L. M.; Lyon, E. J.; Hall, M. B.; Darensbourg, M. Y. *Coord. Chem. Rev.* **2003**, *238*−*239*, 255−266.

10.1021/ic0623361 CCC: $37.00
Published on Web 01/27/2007

system and to calibrate the computational approaches directed toward the elucidation of the enzymatic reaction path.

The enzymatic mechanism of [FeFe] hydrogenase has been investigated using density functional theory (DFT), and two different descriptions have emerged.[7] Either dihydrogen activation occurs at the "vacant" apical site of the iron atom most distant from the 4Fe4S cube of the H cluster,[8,9] in which case the rate of reaction might be accelerated by a bridging dithiomethylamine cofactor,[10] or the reaction occurs opposite the bridging ligand between the two iron atoms of the 2Fe3S subsite.[7,11] Although the facile formation of hydride-bridged compounds by protonation of electron-rich dithiolate-bridged diiron compounds is well documented,[2,12] recent studies by Rauchfuss and co-workers of $[Fe_2(\mu, \mu\text{-}SCH_2CH_2S)H(CO)_2(PMe_3)_4]^+$ show clearly that the form with a bridging hydride is much more inert to protonation and hydrogen elimination than is the isomer with a terminal hydride.[13] Whereas the mechanistic detail of this reaction has not been resolved, the high kinetic activity of hydrogenase enzymes would, at first sight, appear to be inconsistent with formation of a kinetically inert hydride-bridged intermediate.

The current work explores the influence of the 2Fe2X core geometry on electrocatalytic proton reduction. The strategy employed draws on the difference in reduction chemistry for thiolato- and phosphido-bridged compounds where, for the latter, there is a tendency to give a product with a planar 2Fe2P core geometry.[14] For the reduced 2Fe2P species, the core geometry can be constrained by incorporation of a linking group between the phosphorus atoms. The first part of the article is concerned with characterization of the reduction products of the propylene-linked compound. The influence of this structural constraint on the chemistry is then examined with reference to electrocatalytic proton reduction. Differences between the rates of dihydrogen evolution from the doubly reduced and protonated phosphido- and thiolato-bridged diiron compounds is then used to evaluate the influence of the core geometry on the catalytic reaction and to cast light on the reaction path. These results are then considered in the context of the proposed reaction path for the enzyme.

Experimental Details

General Procedures. Samples of $Fe_2(\mu, \mu\text{-}PPh(CH_2)_3PPh)(CO)_6$, **3P** were prepared using literature methods[15] and confirmed to be pure by spectroscopic and electrochemical analyses. Samples of $LiBEt_3H$ (1 M in THF, Aldrich) and *p*-toluenesulfonic acid, HOTs (Merck), were obtained from commercial sources and used without further purification. High-purity argon and nitrogen were obtained from BOC Gases. Solvents were dried using standard procedures[16] and distilled under an atmosphere of dinitrogen immediately prior to use. Solutions used for electrochemical analysis were prepared under a dinitrogen atmosphere either using standard Schlenk techniques or with the aid of a Vacuum Atmospheres glove box. The tetra-*n*-butlyammonium hexafluorophosphate ($TBAPF_6$) used for electrochemical measurements was synthesized and purified using standard procedures.[17]

Electrochemistry and Spectroelectrochemistry (SEC). Cyclic voltammetry experiments were controlled using an Autolab PGSTAT30 potentiostat with GPES software and were carried out in a one-compartment glass cell using a 1-mm vitreous carbon working electrode, double-jacketed silver wire pseudo-reference electrode, and platinum wire counter electrode. The potential of the reference electrode was determined using the ferrocenium/ferrocene (Fc^+/Fc) couple, and all potentials are quoted relative to the SCE reference electrode. Against this reference, the Fc^+/Fc couple occurs at +0.56 V in THF.[18] Electrochemical simulations were carried out using the program Digisim (version 3.03, Bioanalytical Systems).[19]

Spectroelectrochemical experiments were performed using a previously described[20] purpose-built cell. All experiments were conducted using a 3-mm-diameter vitreous carbon working electrode, a silver pseudo-reference electrode, and a platinum foil counter electrode. A PAR model 362 potentiostat was used to control the potential, and a Powerlab 4/20 interface with Chart V4.12 software (ADInstruments) was used to monitor the potential and current response during SEC experiments.

Continuous-flow electrosynthesis experiments were conducted using a cell described in the literature[21] that incorporates reticulated vitreous carbon as the working and counter electrodes and a jacketed silver wire as a pseudo-reference electrode. Standard liquid chromatography fittings in conjunction with narrow-bore (0.2-mm-i.d.) Teflon tubing was used to transfer solutions from the syringe pump to the electrosynthesis cell and then to the sample cells. The extent of electrosynthesis was monitored by IR spectroscopy.

EXAFS Sample Preparation and Analysis. Fe K-edge (7111.2 eV) X-ray absorption measurements were conducted using the bending magnet source of beamline 20B at the KEK Photon Factory Tsukuba, Tsukuba, Japan. A channel-cut Si(111) monochromator with energy resolution ($\Delta E/E$) of ca. 2.4×10^{-4} provided the source of monochromatic radiation, where higher-order harmonics at the selected wavelength were rejected by detuning the monochromator by a factor of $^1/_2$. Solutions were measured in fluorescence mode using a 36-element Ge detector (Canberra). Data analysis was conducted using the XFIT suite of programs,[22] which incorporates FEFF version 6.01.[23] Details of the procedures followed for the

(7) Zampella, G.; Greco, C.; Fantucci, P.; De Gioia, L. *Inorg. Chem.* **2006**, *45*, 4109−4118.
(8) Cao, Z.; Hall, M. B. *J. Am. Chem. Soc.* **2001**, *123*, 3734−3742. Liu, Z.-P.; Hu, P. *J. Chem. Phys.* **2002**, *117*, 8177−8180.
(9) Liu, Z.-P.; Hu, P. *J. Am. Chem. Soc.* **2002**, *124*, 5175−5182.
(10) Fan, H.-J.; Hall, M. B. *J. Am. Chem. Soc.* **2001**, *123*, 3828−3829.
(11) Zhou, T.; Mo, Y.; Liu, A.; Zhou, Z.; Tsai, K. R. *Inorg. Chem.* **2004**, *43*, 923−930. Bruschi, M.; Fantucci, P.; De Gioia, L. *Inorg. Chem.* **2002**, *41*, 1421−149.
(12) Arabi, M. S.; Mathieu, R.; Poilblanc, R. *J. Organomet. Chem.* **1979**, *177*, 199−209.
(13) van der Vlugt, J. I.; Rauchfuss, T. B.; Whaley, C. M.; Wilson, S. R. *J. Am. Chem. Soc.* **2005**, *127*, 16012−16013.
(14) Ginsburg, R. E.; Rothrock, R. K.; Finke, R. G.; Collman, J. P.; Dahl, L. F. *J. Am. Chem. Soc.* **1979**, *101*, 6550−6562.
(15) Collman, J. P.; Rothrock, R. K.; Finke, R. G.; Moore, E. J.; Rose-Munch, F. *Inorg. Chem.* **1982**, *21*, 146−156. Flood, T. C.; DiSanti, F. J.; Campbell, K. D. *Inorg. Chem.* **1978**, *17*, 1643−1646.
(16) Errington, R. J. *Guide to Practical Inorganic and Organo-Metallic Chemistry*; Blackie Academic & Professional: London, 1997.
(17) Sawyer, D. T.; Sobkowiak, A.; Roberts, J. J. L. *Electrochemistry for Chemists*, 2nd ed.; Wiley-Interscience: New York, 1995.
(18) Connelly, N. G.; Geiger, W. E. *Chem. Rev.* **1996**, *96*, 877−910.
(19) Rudolph, M.; Reddy, D. P.; Feldberg, S. W. *Anal. Chem.* **1994**, *66*, 589A−600A.
(20) Borg, S. J.; Best, S. P. *J. Electroanal. Chem.* **2002**, *535*, 57−64.
(21) Bondin, M. I.; Foran, G.; Best, S. P. *Aust. J. Chem.* **2001**, *54*, 705−709.
(22) Ellis, P. J. *Xfit for Windows 95*; Australian Synchrotron Research Program: Sydney, Australia, 1996. Ellis, P. J.; Freeman, H. C. *J. Synchrotron Radiat.* **1995**, *2*, 190−195.
(23) Zabinsky, S. I.; Rehr, J. J.; Ankudinov, A.; Albers, R. C.; Eller, M. J. *Phys. Rev. B: Condens. Matter Phys.* **1995**, *52*, 2995−3009.

analysis of related systems have been described previously.[5,24,25] Samples of the reduced compounds were generated by continuous-flow electrosynthesis using 5 mM (i.e., 10 mM in Fe) solutions of **3P** in THF/0.2 M TBA[PF_6]. The potential of the cell was controlled using a PAR model 273A potentiostat, and the composition of the solution was monitored, in line, by IR spectroscopy (Shimadzu, Prestige), with the sample freeze-quenched in liquid nitrogen.

Instrumentation. IR SEC spectra were collected using a Biorad FT175C FTIR spectrometer with a Ge/KBr beamsplitter and a narrow-band MCT detector. Spectral subtraction and curve fitting was performed using Grams/32 AI software (Galactic). Multicomponent analysis was conducted using routines available within the program Igor Pro (version 5.04B, Wavemetrics). A Bruker ECS106 X-band spectrometer was used to collect EPR spectra.

DFT Calculations. All reported calculations were conducted using the hybrid functional B3LYP as implemented in the Gaussian 03 (G03, revision B.04) package[26] using the all electron basis set 6-311+G(d) with diffuse and polarization functions from the internal library of G03. Calculations were conducted on an analogue of **3P** in which the phenyl rings were replaced by methyl groups. This simplification significantly reduced the time needed for the calculations to reach convergence. Although a similar outcome might have been obtained by restricting the conformational freedom of the phenyl rings, previous calculations[27] suggested that methyl substitution provides a satisfactory alternative. The calculated analogue of **3P** is designated [$\mathbf{3P_M}$], where the subscript indicates the replacement of the phenyl by methyl groups and the square brackets designate a DFT-calculated species. All calculations were performed as restricted spin singlets except for [$\mathbf{3P_M}^-$], which was treated as an unrestricted spin doublet. The crystal structure of **3P** was used as input for geometry optimization of [$\mathbf{3P_M}$]; subsequent optimization of [$\mathbf{3P_M}^-$] proceeded from the optimized geometry of [$\mathbf{3P_M}$] with addition of a single electron specified and no further constraints. Repeating the same procedure gave [$\mathbf{3P_M}^{2-}$]. Vibrational analyses were carried out as second derivatives and confirmed that all optimized geometries were true minima.

Solvation effects were included using the PCM model[28] as implemented in G03 with THF as the implicit solvent. Molecular cavities were built as solvent-excluding surfaces using the United Atom Topological Model and atomic radii optimized for the PBE0/6-31G(d) level of theory. All final geometry optimizations and subsequent vibrational analyses were conducted within the PCM framework described above.

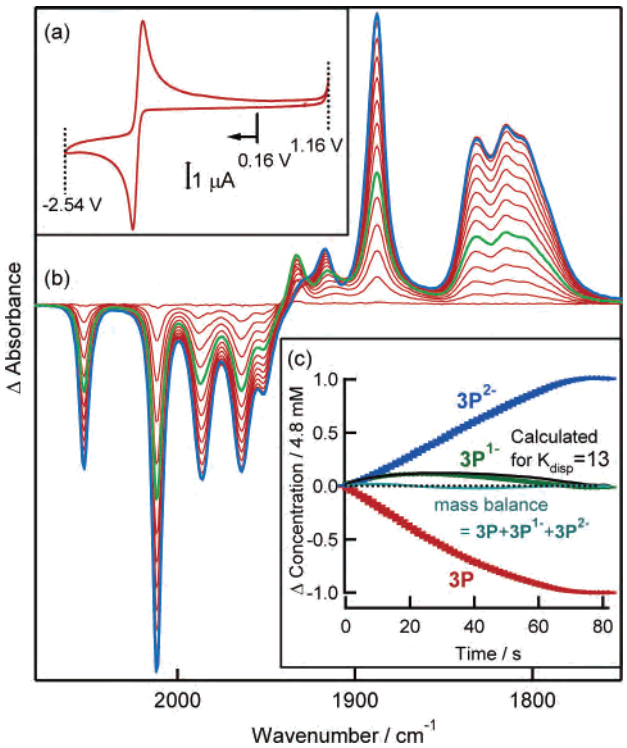

Figure 1. (a) Cyclic voltammogram (100 mV/s) of **3P** in THF/0.2 M $TBAPF_6$ (all potentials are given with reference to the SCE). (b) Differential absorption IR spectra recorded during reduction of a 4.8 mM solution of **3P** in THF/0.2 M $TBAPF_6$. Spectra were recorded with a 1.5-s interval following a potential step from 0 to −1.8 V where, for clarity, every fourth spectrum is shown. (c) Time dependence of the concentrations of **3P**, $\mathbf{3P}^-$, and $\mathbf{3P}^{2-}$ obtained by fitting the SEC spectra. The solid line corresponds to the concentration of $\mathbf{3P}^-$ calculated using the concentrations of **3P** and $\mathbf{3P}^{2-}$ and an equilibrium constant of 13 for the disproportionation of $\mathbf{3P}^-$.

Results and Discussion

Electrochemistry of 3P. The electrochemical response of **3P** is similar to that of $Fe_2(\mu\text{-}PPh_2)_2(CO)_6$, **DP**, described previously.[25] The assignment of the single reduction wave (−1.52 V, Figure 1a) to a two-electron process is suggested by the relative magnitudes of the peak anodic and cathodic currents relative to that obtained for oxidation of an equimolar solution of ferrocene when measured in the same experiment and is corroborated by the magnitude of the charge transferred during exhaustive electrosynthesis of the thin layer during SEC experiments (2.2 ± 0.2 electrons/molecule). The conclusion is supported by analysis of the IR-active ν(CO) bands of the reduction product, $\mathbf{3P}^{2-}$, described in the next section. Whereas alkali metal reduction also yields solutions of $\mathbf{3P}^{2-}$, it has not proved possible to obtain a sample of this species in a form suitable for X-ray structural characterization. Although the assignment of the two-electron character of the reduction process of **3P** is unambiguous, the value of ΔE_p (ca. 137 mV, 100 mV s^{-1}) in THF is substantially larger than that obtained for the Fc^+/Fc couple (78 mV) when measured under the same conditions. This indicates that the process does not involve

(24) Bondin, M. I.; Borg, S. J.; Cheah, M. H.; Foran, G.; Best, S. P. *Aust. J. Chem.* **2006**, *59*, 263−272.
(25) Cheah, M. H.; Borg, S. J.; Bondin, M. I.; Best, S. P. *Inorg. Chem.* **2004**, *43*, 5635−5644.
(26) Frisch, M. J.; Trucks, G. W.; Schlegel, H. B.; Scuseria, G. E.; Robb, M. A.; Cheeseman, J. R.; Montgomery, J. A., Jr.; Vreven, T.; Kudin, K. N.; Burant, J. C.; Millam, J. M.; Iyengar, S. S.; Tomasi, J.; Barone, V.; Mennucci, B.; Cossi, M.; Scalmani, G.; Rega, N.; Petersson, G. A.; Nakatsuji, H.; Hada, M.; Ehara, M.; Toyota, K.; Fukuda, R.; Hasegawa, J.; Ishida, M.; Nakajima, T.; Honda, Y.; Kitao, O.; Nakai, H.; Klene, M.; Li, X.; Knox, J. E.; Hratchian, H. P.; Cross, J. B.; Bakken, V.; Adamo, C.; Jaramillo, J.; Gomperts, R.; Stratmann, R. E.; Yazyev, O.; Austin, A. J.; Cammi, R.; Pomelli, C.; Ochterski, J. W.; Ayala, P. Y.; Morokuma, K.; Voth, G. A.; Salvador, P.; Dannenberg, J. J.; Zakrzewski, V. G.; Dapprich, S.; Daniels, A. D.; Strain, M. C.; Farkas, O.; Malick, D. K.; Rabuck, A. D.; Raghavachari, K.; Foresman, J. B.; Ortiz, J. V.; Cui, Q.; Baboul, A. G.; Clifford, S.; Cioslowski, J.; Stefanov, B. B.; Liu, G.; Liashenko, A.; Piskorz, P.; Komaromi, I.; Martin, R. L.; Fox, D. J.; Keith, T.; Al-Laham, M. A.; Peng, C. Y.; Nanayakkara, A.; Challacombe, M.; Gill, P. M. W.; Johnson, B.; Chen, W.; Wong, M. W.; Gonzalez, C.; Pople, J. A. *Gaussian 03*, revision B.04; Gaussian, Inc.: Wallingford CT, 2004.
(27) Baik, M.-H.; Ziegler, T.; Schauer, C. K. *J. Am. Chem. Soc.* **2000**, *122*, 9143−9154.
(28) Cammi, R.; Mennucci, B.; Tomasi, J. *J. Phys. Chem. A* **1999**, *103*, 9100−9108. Cammi, R.; Mennucci, B.; Tomasi, J. *J. Phys. Chem. A* **2000**, *104*, 5631−5637. Mennucci, B.; Cances, E.; Tomasi, J. *J. Phys. Chem. B* **1997**, *101*, 10506−10517. Mennucci, B.; Tomasi, J. *J. Chem. Phys.* **1997**, *106*, 5151−5158.

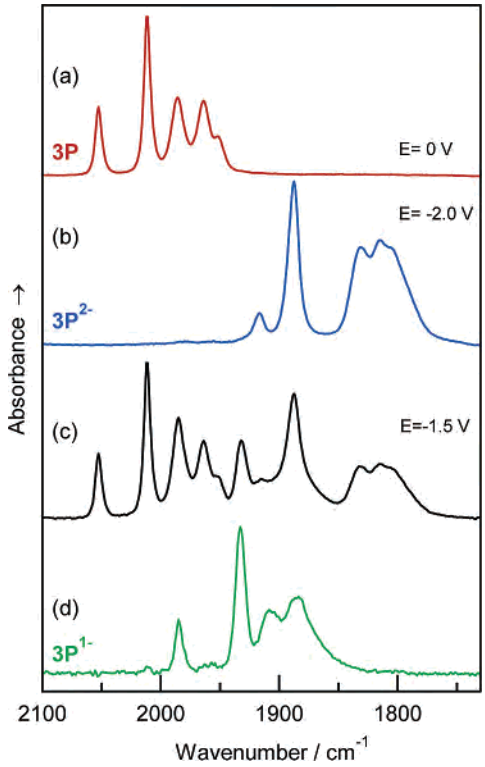

Figure 2. Representative IR spectra recorded from a solution of **3P** in THF/TBAPF$_6$ following continuous-flow electrosynthesis at potentials of (a) 0, (b) −2.0, and (c) −1.5 V and (d) the spectrum of **3P**$^-$ obtained by the subtraction of the spectra of **3P** and **3P**$^{2-}$ from that obtained at potentials near −1.5 V.

diffusion-controlled electron transfer, for which ΔE_p can, for example, be modeled by a process involving two one-electron steps where the rate of electron transfer is low for one of the steps.

Spectroelectrochemistry (SEC) of 3P. Reduction of **3P** in THF at −1.8 V in a thin-layer SEC experiment leads to quantitative formation of a well-defined product, **3P**$^{2-}$, with an IR spectrum similar to that of the crystallographically characterized complex **DP**$^{2-}$ (Figure 1b). The process is chemically reversible, with near quantitative recovery of the starting material obtained by application of a potential of ca. −1.0 V (Figure S1). The absence of an isosbestic point in the spectra recorded during reduction indicates the formation of significant concentrations of at least one other species during the conversion, where the transient appearance of a band near 1940 cm^{-1} (Figure 1b) provides a clear marker of such an intermediate. The IR spectrum of this species can be extracted from the differential absorption SEC spectra. The spectral profile of the intermediate is closely related to that of the starting material but shifted to lower wavenumber (Figure 2), suggesting retention of the core geometry with the shift of the ν(CO) bands consistent with formation of the one-electron-reduced species, **3P**$^-$. The spectra recorded during reduction can be satisfactorily fitted to a combination of the spectra of **3P**, **3P**$^-$, and **3P**$^{2-}$ (Figure 1c) with no other species formed in significant concentrations. Although mixing of the solution in the thin layer might complicate the analysis, the observed concentration of **3P**$^-$ is well modeled by the disproportionation equilibrium of **3P**$^-$ (eq 1) with K_{disp} = 13, where the value of K_{disp} was obtained from continuous-flow electrosynthesis experiments described in the following section. It is noted that the spectrum of **3P**$^{2-}$ obtained by subtraction is contaminated by a small concentration of **3P**$^-$, and this accounts for the poorer agreement between the observed and calculated concentrations of **3P**$^-$ at longer times. Experiments conducted at lower temperatures did not give a more pronounced initial increase in the concentration of **3P**$^-$, and this supports the proposition that the neutral, monoanion, and dianion are in thermodynamic equilibrium. Corresponding experiments conducted in CH_3CN showed a similar conversion of **3P** to **3P**$^{2-}$, although without the formation of significant concentrations of **3P**$^-$ (Figure S2).

$$2\ \mathbf{3P}^- \rightleftharpoons \mathbf{3P} + \mathbf{3P}^{2-} \qquad K_{disp} \qquad (1)$$

Analysis of the SEC results suggests that 3P$^-$ might be formed by comproportionation of **3P** and **3P**$^{2-}$. Support for this proposition is provided by continuous-flow electrosynthesis experiments in which the products are monitored, in line, by IR spectroscopy. Spectra recorded at the resting potential, at potentials sufficient to give quantitative conversion to **3P**$^{2-}$ and near the half-wave potential, are shown in Figure 2. The spectrum of the intermediate product, **3P**$^-$, can be obtained by subtraction (Figure 2d). The IR spectra generated from the continuous-flow electrosynthesis experiments match closely those extracted from the in situ SEC experiments (Figure 1). Analysis of the IR spectra indicates that the composition of the solution has a **3P**/**3P**$^-$/**3P**$^{2-}$ ratio of 43:12:45, which gives K_{disp} = 13. This result is consistent with the analysis of the SEC spectra (Figure 1c). The value of K_{disp} requires that the reduction potential of **3P** is 67 mV more negative than that of **3P**$^-$. In cases where the applied potential is such as to give approximately equal concentrations of **3P** and **3P**$^{2-}$, the relative concentration of **3P**$^-$ does not change significantly if the flow rate of the solution (i.e., the time between electrosynthesis and collection of the IR spectrum) is changed. Moreover, if the flow from the electrosynthesis cell is diverted so as to give a static solution in the IR cell, then the relative concentrations of the three species are found not to change to a significant extent over a 10-min period.

The monomeric form of **3P**$^-$ is suggested both by the IR spectrum and by the observation of a strong EPR signal from a THF solution obtained by mixing equimolar amounts of **3P** and **3P**$^{2-}$, where the latter was obtained by sodium reduction. At room temperature, a single resonance was observed in which the hyperfine coupling to ^{31}P was not resolved. An identical room-temperature EPR spectrum was obtained from solutions generated by continuous-flow electrosynthesis, where this approach allows the composition of the solution to be established by IR spectroscopy. EPR spectra recorded from these solutions give a single resonance at room temperature (g_{iso} = 1.995, Figure S3) and a rhombic spectrum for frozen solutions (g_1 = 1.985, g_2 = 1.994, g_3 = 2.018). Hyperfine coupling to ^{31}P, a(^{31}P), is evident for each of the components of g (Figure 3). The g value obtained for **3P**$^-$ is similar to that reported for [Fe$_2$(μ-PMe$_2$)$_2$(CO)$_6$]$^{1-}$ (g_{iso}

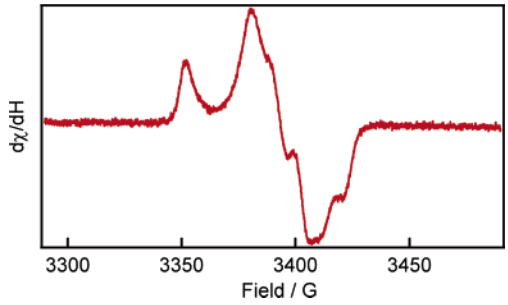

Figure 3. X-band EPR spectrum recorded from a frozen solution (120 K) of partly reduced **3P** THF/$TBAPF_6$ prepared by continuous-flow electrosynthesis.

= 1.999),[29] and the apparently small value of $a(^{31}P)$ is consistent with the more highly resolved spectrum reported in a subsequent study [$a(^{31}P) = 4.5$ G and $a(^{1}H) = 1.4$ and <0.2 G].[30] The EPR spectrum reported for $[Fe_2(\mu\text{-}P(Bu^t)_2)_2(CO)_5]^{1-}$, a decarbonylated analogue of $\mathbf{3P}^-$ that features an Fe−Fe double bond, has a g_{iso} value of 2.037 and an $a(^{31}P)$ value of 14.7 G.[31] Hyperfine coupling to the protons of the carbon atom bound directly to the P atom was not resolved in the spectra. More extensive studies of diiron compounds bridged by a single phosphido group, $Fe_2(\mu\text{-}PR_2)(CO)_7$, give values of g_{iso} close to 2.05 and $a(^{31}P)$ of ca. 23 G, whereas the hyperfine coupling to the protons of the dialkylphosphido bridged compounds could not be resolved.[32,33] In addition to the structure in the frozen EPR spectrum, retention of the two phosphorus atoms at the diiron core of $\mathbf{3P}^-$ is supported by the transient (ca. 30 min) observation of a three-line EPR spectrum immediately following introduction of low concentrations of dioxygen; addition of dioxygen to $\mathbf{3P}^-$ or $\mathbf{3P}^{2-}$ results in solutions containing **3P**. The three-line pattern is well simulated by a doublet of doublets with a g_{iso} value of 2.045 and $a(^{31}P)$ values of 19.1 and 11.7 G. The inequivalence of the two phosphorus atoms of the oxidation product of $\mathbf{3P}^-$ might reflect a change in the coordination geometry as would occur if one of the P atoms adopted a terminal mode of coordination. The EPR spectrum of $[FeCo(\mu\text{-}PPh_2)(CO)_6(PPh_3)]^+$ gives a three-line spectrum, which, although reported as a triplet,[33] can also be simulated by a doublet of doublets.

EXAFS of the 3P Redox Series. In the absence of crystalline samples suitable for X-ray crystallographic analysis, the basic details of the core geometry of the reduced forms of **3P** can be obtained using EXAFS techniques. The EXAFS data of 5 mM THF solutions of **3P** and $\mathbf{3P}^{2-}$ have been modeled using approaches described in a recent work,[24] and the results are summarized in Table 1. In the case of **3P**, it is possible to verify the accuracy of the derived parameters, which are in excellent agreement with those obtained crystallographically.[34] As expected, there is a substantial increase in the Fe−Fe distance following reduction, although the resulting value is shorter for $\mathbf{3P}^{2-}$ than for $\mathbf{DP}^{2-}$. Although these measurements provide good estimates of the Fe−Fe and Fe−P distances, there are no multiple-scattering paths that are sufficiently close to linear (Fe−P−X angle >150°) to make a significant contribution to the scattering to allow definition of the 2Fe2P core geometry. Although the P−P separation, from P K-edge EXAFS spectra, would resolve this problem, measurements in the required energy range (2.14 keV) are not possible using beamline 20B.

Table 1. EXAFS Parameters and Refinement Statistics[a]

	3P	$\mathbf{3P}^{2-}$
E_0/eV (S_0^2)	−7.97 (0.78)	−12.87 (0.73)
χ^2 (R_{EXAFS}/%)	1.67 (10.28)	3.14 (14.99)
Fe−Fe/Å	2.63 (0.0015)[b] [2.630]	3.55 (0.0011)
Fe−μ-P/Å	2.21 (0.0013) [2.212[c]]	2.23 (0.0015)
Fe−C(O)/Å	1.78 (0.0013) [1.791[c]]	1.75 (0.0008)
C−O/Å	1.16 (0.0028) [1.140[c]]	1.16 (0.0031)
P−C_α/Å	1.87 (0.0009) [1.828[c]]	1.60 (0.0031)

[a] A total of 13 independent parameters were refined over the range 1−13 $Å^{-1}$ in k and 1−4 Å in R (25 independent points[35]). Details of the refinement parameters are given in Table S1, and plots of the observed and calculated EXAFS spectra are shown in Figure S4. Definitions of χ^2 and R_{EXAFS} are given in ref 25. [b] Debye−Waller factors ($Å^2$) are given in parentheses, and X-ray-determined values[34] are given in square brackets. The error in the internuclear contacts is dominated by the typical systematic error, assigned a conservative consensus value of 0.02 Å.[36] [c] Average value.

The product distribution obtained from electrochemical and chemical reduction of **3P** indicates that the disproportionation equilibrium is rapidly established, and this limits the concentration of $\mathbf{3P}^-$ available in solution. Even in THF, where the relative stability of $\mathbf{3P}^-$ is greatest, the maximum relative concentration of the anion amounts to only ca. 12% of the total concentration of the **3P** species. In this case, the range of structural information for $\mathbf{3P}^-$ that can be extracted from EXAFS analysis is restricted to the determination of the Fe−Fe distance.

Two solutions having approximately equal concentrations of **3P** and $\mathbf{3P}^{2-}$ were used for collection of Fe K-edge X-ray absorption spectra. IR analysis indicates the presence of approximately 12% of $\mathbf{3P}^-$ for both solutions (Figure 2). The simplest and most highly constrained method for extracting the Fe−Fe separation for $\mathbf{3P}^-$ involves modeling the data using the EXAFS-derived structural parameters for the neutral and dianion forms with the populations of these species fixed according to the composition determined using IR spectroscopy. A single Fe−Fe interaction with population fixed at 0.12 requires two parameters, and these, together with E_0 and S_0^2 were refined. In cases where the initial Fe−Fe distance was in the range of 2.8−3.4 Å, the refinement proceeded to local minima with refined Fe−Fe distances of 2.76, 3.03, and 3.26 Å. The analysis was repeated using several different relative populations of **3P** and $\mathbf{3P}^{2-}$ with ratios ranging between 40:48 and 48:40, and this showed

(29) Dessy, R. E.; Kornmann, R. L.; Smith, C.; Haytor, R. *J. Am. Chem. Soc.* **1968**, *90*, 2001−2004.
(30) Dessy, R. E.; Rheingold, A. L.; Howard, G. D. *J. Am. Chem. Soc.* **1972**, *94*, 746−752.
(31) van der Linden, J. G. M.; Heck, J.; Walther, B.; Boettcher, H. C. *Inorg. Chim. Acta* **1994**, *217*, 29−32.
(32) Baker, R. T.; Krusic, P. J.; Calabrese, J. C.; Roe, D. C. *Organometallics* **1986**, *5*, 1506−1508.
(33) Baker, R. T.; Calabrese, J. C.; Krusic, P. J.; Therien, M. J.; Trogler, W. C. *J. Am. Chem. Soc.* **1988**, *110*, 8392−8412.
(34) Reingold, A. L. *Acta Crystallogr. C: Cryst. Struct. Commun.* **1985**, *41*, 1043.
(35) Stern, E. A. *Phys. Rev. B* **1993**, *48*, 9825−9827.
(36) Gurman, S. J. *J. Synchrotron Radiat.* **1995**, *2*, 56−63.

Table 2. Summary of the Final Refinement Parameters from DFT Structure Optimization for the [**3P**$_M$] Redox Series

	[**3P**$_M$]	[**3P**$_M^-$]	[**3P**$_M^{2-}$]
Fe−Fe/Å	2.677	3.142	3.638
Fe−P[a]/Å	2.257	2.299	2.334
Fe−CO$_{ap}$[a]/Å	1.775 [1.768][b]	1.783	1.754[c]
Fe−CO$_{bas}$[a]/Å	1.800 [1.787]	1.779	
P−P/Å	2.803 [2.742]	2.724	2.591
dihedral[d]	98.3 [98.5]	116.0	139.2

[a] Average value. [b] X-ray value.[34] [c] Apical/basal positions are not defined for [3P$_M^{2-}$]. [d] Defined as the Fe−P−P−Fe dihedral angle.

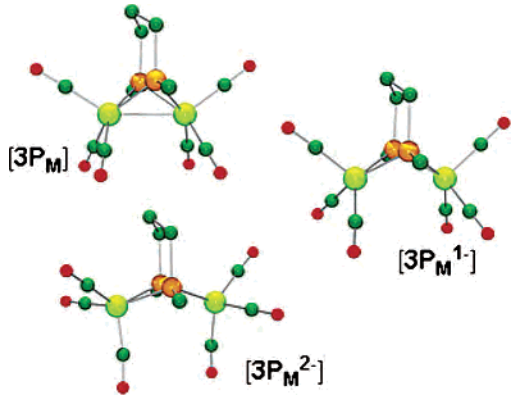

Figure 4. DFT-optimized structures of the **3P**$_M$ redox series; for clarity, the hydrogen stoms have been omitted.

that the final Fe−Fe distance is not correlated with the solution composition (Table S2).

DFT Calculations of the 3P Redox Series. Geometry optimization of [**3P**$_M$], [**3P**$_M^-$], and [**3P**$_M^{2-}$] proceeded to give well-defined minima with the structures shown in Figure 4 and selected structural parameters given in Table 2. For related dithiolato-bridged compounds, the reliability of the calculations for prediction of the structure and IR spectra is well established,[7,8,37−39] and the extension of this approach to the linked phosphido-bridged compound was assessed with reference to **3P**. There is close agreement between the details of the X-ray and calculated structure, including the small difference in Fe−C bond lengths for the basal and apical CO groups and the 2Fe2P dihedral angle (Table 2). The discrepancy between the Fe−Fe (0.048 Å) and Fe−P (0.046 Å) distances are basis-set-dependent, and the systematic overestimation of these distances by ca. 0.05 Å for the neutral compound is in keeping with earlier observations.[24] The good agreement between the observed and computed spectra (Figures 5 and S5) is in keeping with recent studies of the correlation between the computed and observed IR spectra in the ν(CO) region.[37,39] The different scaling factor that would apply for the present study relative to that reported

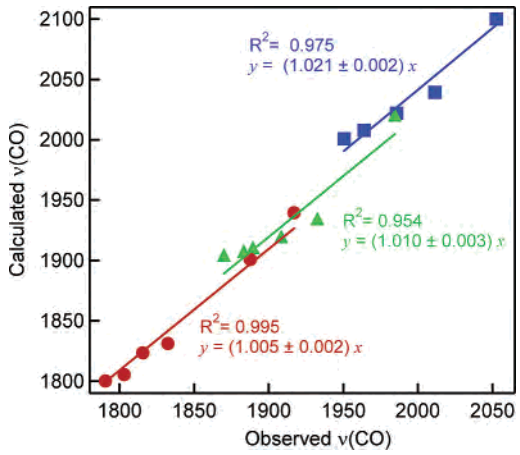

Figure 5. Comparison of the wavenumbers of the IR-active ν(CO) bands of **3P** (■), **3P**$^-$ (▲), and **3P**$^{2-}$ (●)

by Tye et al.[39] most likely reflects differences in the basis sets and inclusion of solvation effects in the present study.

Although X-ray data are not available for **3P**$^{2-}$, previous investigations have shown that this level of theory gives very satisfactory results for the related compound, **DP**$^{2-}$, for which the calculated Fe−Fe distance is within 0.1 Å of that obtained crystallographically.[14, 27] After the systematic differences in the calculated bond lengths have been taken into consideration, there is good agreement between the EXAFS-derived Fe−Fe and Fe−P bond lengths (Δr = 0.089 and 0.103 Å) for **3P**$^{2-}$ (Tables 1 and 2), and there is excellent agreement between the calculated and observed ν(CO) IR spectra (Figure 5).

For **3P**$^-$, the Fe−Fe distance is poorly defined by the EXAFS analysis and gives an estimate of ca. 3.1 Å. In terms of the uncertainty associated with the extraction of this parameter from the EXAFS spectrum of a species that represents a minor component of the sample, the agreement between the calculated and experimental Fe−Fe distances for **3P**$^-$ is considered to be satisfactory. Further validation of the calculations is obtained from the good agreement between the calculated and observed IR spectra (Figure 5).

It is apparent from the calculated structures that the propylene linking group severely impacts the geometry of the dianion and the large increase in Fe−Fe distance is accommodated by a highly distorted structure (Figure 4). Clearly, the propylene linker prevents the 2Fe2P core from adopting a planar arrangement, with the dihedral angle of the butterfly increasing from 98° for [**3P**$_M$] to 139° for [**3P**$_M^{2-}$]; a dihedral angle of 180° is obtained for the planar core geometry of **DP**$^{2-}$.[14] The coordination environment about each Fe center was calculated to be approximately square-pyramidal, with one of the CO groups in the apical position and distortion of the basal positions resulting from a P−Fe−P angle of 67.5°. The C atoms bound directly to the bridging P have significantly different nonbonded contacts to the Fe atoms (3.400 and 3.625 Å), and additionally, there is one Fe−Fe−C(O) angle close to 90° for each Fe atom, giving an additional nonbonded contact closer than 4 Å. The simple model used to fit the EXAFS data does not allow for distortions of this sort and, if reflected in the

(37) Zilberman, S.; Stiefel, E. I.; Cohen, M. H.; Car, R. *J. Phys. Chem. B* **2006**, *110*, 7049−7057.
(38) Zampella, G.; Bruschi, M.; Fantucci, P.; Razavet, M.; Pickett, C. J.; De Gioia, L. *Chem.-Eur. J.* **2005**, 11, 509−520. Fiedler, A. T.; Brunold, T. C. *Inorg. Chem.* **2005**, *44*, 1794−1809. Fiedler, A. T.; Brunold, T. C. *Inorg. Chem.* **2005**, *44*, 9322−9334. Bruschi, M.; Zampella, G.; Fantucci, P.; De Gioia, L. Coord. *Chem. Rev.* **2005**, *249*, 1620−1640.
(39) Tye, J. W.; Darensbourg, M. Y.; Hall, M. B. *J. Comput. Chem.* **2006**, 27, 1454−1462. Borg, S. J.; Tye, J. W.; Hall, M. B.; Best, S. P. *Inorg. Chem.* **2007**, *46*, 384−394.

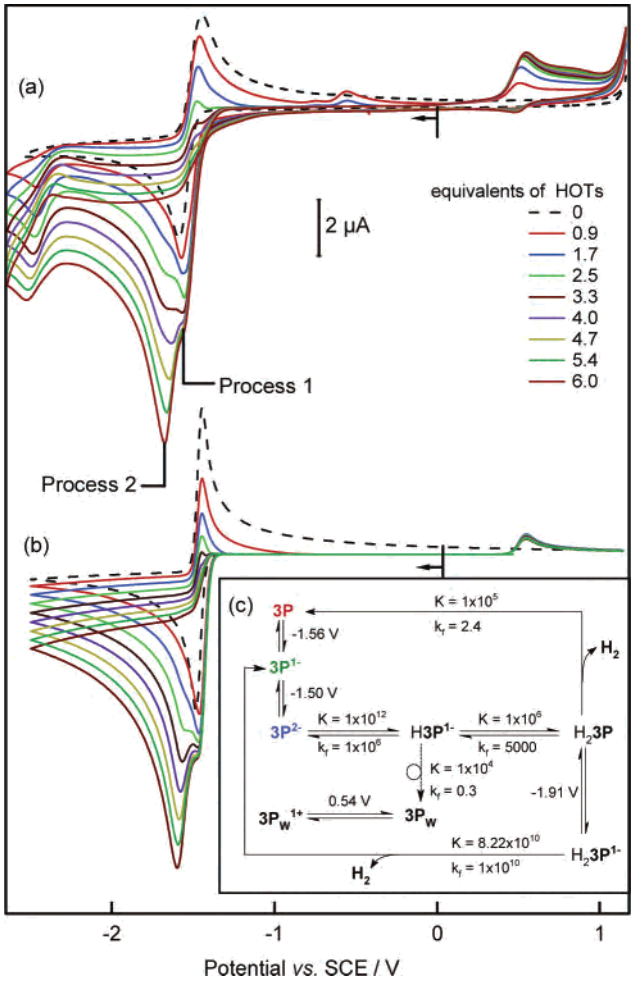

Figure 6. (a) Cyclic voltammetry of **3P** (1.15 mM) in THF/0.2 M $TBAPF_6$ with 0−6 equiv of HOTs and (b) Digisim[19] simulation of the electrochemistry based on the scheme given in the inset (c). Full details of the simulation parameters are given in Table S3.

structure of $\mathbf{3P}^{2-}$, would contribute to the poorer fit obtained for modeling of the EXAFS data of $\mathbf{3P}^{2-}$ relative to $\mathbf{DP}^{2-}$. A small improvement in the refinement statistics for the EXAFS modeling of $\mathbf{3P}^{2-}$ was obtained by elaboration of the model to allow for these distortions; however, the improvement was not sufficient to allow assignment of these details of the structure.

Electrocatalytic Proton Reduction by 3P. Reduction of **3P** in the presence of HOTs is accompanied by well-defined electrocatalytic proton reduction waves with E_{pc} equal to −1.55 V (process 1) and −1.68 V (process 2) that dominate at low and high acid concentrations, respectively, together with an additional weak feature with E_{pc} equal to −2.5 V (Figure 6a). The voltammetry of **3P** in the presence of HOTs can be modeled satisfactorily using the scheme shown in Figure 6c. At low acid concentrations, an EECC mechanism[40] operates in which two one-electron transfer (E) steps precede the chemical steps (C) where these involve protonation (×2) and dihydrogen elimination. The difference in potential for reduction of **3P** and $\mathbf{3P}^{-}$ is fixed by the value of K_{disp}. Although a contribution to the reaction path from sequential electron/proton additions as proposed[5] for $Fe_2(\mu,\mu\text{-}S(CH_2)_3S)(CO)_6$ (**3S**) is not ruled out by this analysis, the additional complication is not required for satisfactory modeling of the voltammetry. The electrocatalytic current is limited by the low rate of dihydrogen elimination from $H_2\mathbf{3P}$, and further reduction of this species results in rapid evolution of dihydrogen.

It is important to note that electrocatalytic proton reduction by **3P** is markedly different from that of **DP**, where addition of HOTs shifts the potential of the primary reduction wave but no electrocatalytic response is obtained.[25] The current response of **3P** is similar to that of **3S**, in which dihydrogen evolution follows two-electron reduction of the complex in acid with more rapid dihydrogen evolution following further reduction.[5] The dependence on acid concentration of the current at the potential of the primary reduction process provides a measure of the relative rates of dihydrogen elimination from the two-electron, two-proton products. Under dinitrogen and comparable conditions of scan rate and concentration, the ratio of the current obtained for **3S** in the presence and absence of 6 equiv of HOTs is 4.4, whereas for **3P**, the ratio is 1.7 [although, in the latter case, the two-electron character of the process suggests that doubling the ratio (to 3.4) is more appropriate]. In either case, the difference in catalytic current obtained for process 1 indicates a lower rate for dihydrogen elimination from $H_2\mathbf{3P}$ than from $H_2\mathbf{3S}$. Electrochemical simulation allows quantification of the rate constants and suggests a difference of nearly a factor of 2 for the first-order rate constants.

The reaction path given in Figure 6c allows for loss of the catalyst through rearrangement of $H\mathbf{3P}^{-}$ such that there is no loss or gain of CO associated with formation of $\mathbf{3P_W}$. Consistent with this proposal, addition of CO does not lead to a significant change in the current response for the electrocatalytic reaction. This observation is in contrast to that found for **3S** for which there is strong inhibition of electrocatalysis by CO.[5] In that case, the predominant side product of the reaction is a rearranged 7-CO species $[Fe_2(\mu\text{-}S(CH_2)_3SH)(\mu\text{-}CO)(CO)_6]^{1-}$.

SEC of 3P during Proton Reduction. The current and spectroscopic responses to reduction and reoxidation of a solution containing **3P** with 10 equiv of HOTs are shown in Figure 7. During the initial period of reduction (<45 s), there is a significant current flow, but there is virtually no spectroscopic change (Figure 7a). Analogous experiments conducted in the absence of **3P** show a much slower depletion of the bands due to HOTs (<10%) for final reduction potentials in the range from −1.6 to −2.2 V. These observations require that the catalytic process includes the neutral complex, i.e., dihydrogen evolution occurs from the doubly reduced form of **3P**. These results are in sharp contrast to those obtained with **DP**, for which proton reduction requires access to the three-electron-reduced level and elimination of dihydrogen results in reduced forms of **DP**.[25]

As the HOTs concentration becomes depleted, a weak additional set of bands appear transiently in the spectra with wavenumbers and band profile similar to those of $H_2\mathbf{DP}$

(40) Bard, A. J.; Faulkner, L. R. *Electrochemical Methods: Fundamentals and Applications*; Wiley: New York, 1980.

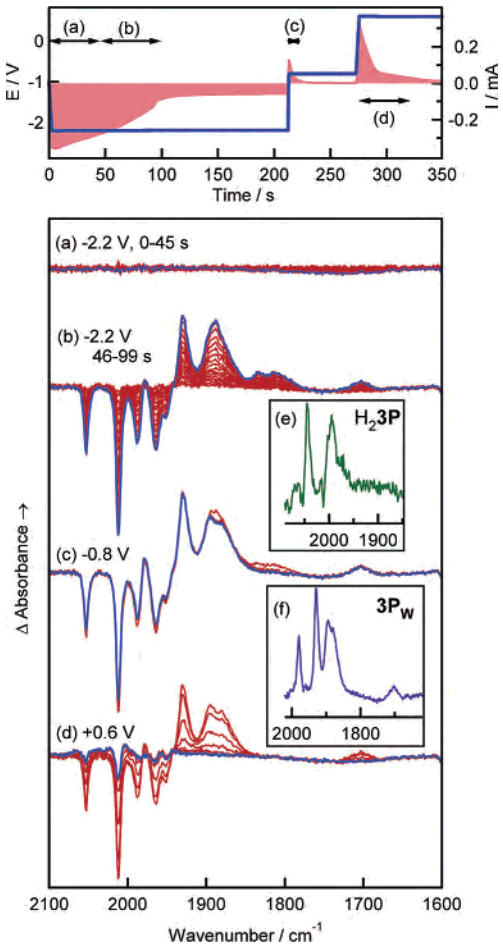

Figure 7. Top: Applied potential and current response from the SEC experiment conducted on a sample of **3P** with 10 equiv of HOTs. The current is displayed as "fill to zero". Bottom: (a−d) Differential absorbance IR spectra recorded during the SEC experiment with the last spectrum of each group highlighted. Spectra of additional species obtained by subtraction of **3P** and $\mathbf{3P}^{2-}$ from the SEC results (e) during the latter stages of reduction at −2.2 V and (f) immediately prior to oxidation at +0.6 V.

(Figure 7e).[25] During this period, there is gradual conversion of **3P** into two predominant products that are identified as $\mathbf{3P_W}$ and $\mathbf{3P}^{2-}$ (Figure 7b). The initial product, $\mathbf{3P_W}$, has an IR band at 1705 cm^{-1}, suggesting rearrangement to give a product with a bridging CO group. The ν(CO) band profile is closely related to that of a previously identified protonated two-electron-reduced product of **DP** (Figure 7f).[25] The geometry proposed for $\mathbf{3P_W}$ has bridging CO and phosphido groups and a terminally bound phosphine ligand. A more detailed study of the characterization of the structure and chemistry of $\mathbf{3P_W}$ is to be the subject of a separate publication. Formation of $\mathbf{3P}^{2-}$ occurs at longer times when the proton concentration in the thin layer is sufficiently low. Application of a potential of −1.0 V leads to selective oxidation of $\mathbf{3P}^{2-}$ with recovery of **3P** (Figure 7c). More positive potentials are required to oxidize $\mathbf{3P_W}$, and this leads to recovery of ca. 90% of the **3P** present at the start of the experiment (Figure 7d).

DFT Investigation of $H_2$3P. Insight into the structure of H_2**3P** can be gained from an earlier ^{1}H NMR study of $H_2Fe_2(\mu\text{-}P(CF_3)_2)_2(CO)_6$, H_2**FP**, which indicated that the hydride ligands are bound to different Fe atoms and occupy coordination sites normal to the 2Fe2P plane.[41] Both cis and trans isomers are obtained, in a relative population of 5:9. The two strong IR bands reported for the compound (2095 and 2054 cm^{-1}) match well the spectra reported for H_2**DP** (2069 vw, 2053 vs, 2007 s, and 2001 s)[25] and H_2**3P** (Figure 7e), where the wavenumber shift is explained in terms of the strongly electron-withdrawing CF_3 groups. In the case of $\mathbf{3P}^{2-}$, protonation would give a canted edge-shared bioctahedral geometry with CO and H ligands occupying the axial sites of each Fe atom. These coordination sites are distinguished according to whether the hydrogen atoms are opposite (down) or adjacent (up) to the propylene group linking the phosphorus atoms. Three isomers based on this geometry are distinguished: up:up, up:down, and down:down. DFT-based geometry optimization proceeded from [$\mathbf{3P_M}^{2-}$] with an additional proton added in a position bridging the two Fe atoms. The final geometry for [H$\mathbf{3P_M}$]$^-$ had a terminally bound hydride in an axial position where up-[H$\mathbf{3P_M}^-$] was calculated to be more stable than down-[H$\mathbf{3P_M}^-$] by 2.75 kcal mol^{-1}. Geometry optimization following addition of a second proton proceeded to well-defined minima for each of the isomers of [H_2**3P**$_M$], with selected structural parameters reported in Table 3. The calculated IR spectra of the isomers of [H_2**3P**$_M$] have band profiles similar to each other and to that of the additional species formed during reduction in the presence of HOTs (Figures 7e and S6). The offset between the observed and calculated ν(CO) frequencies is similar to that obtained for the corresponding modes of **3P**.

Table 3. Summary of the Final Parameters from DFT Structural Refinement of the Isomers of [H_2**3P**$_M$] and *cis*-[H_2**DP**$_M$]

	[H_2**3P**$_M$]			
	down:down	up:down	up:up	*cis*-[H_2**DP**$_M$]
ΔG/(kcal mol^{-1})	2.63	0	1.55	
Fe−Fe/Å	3.619	3.621	3.653	3.634
Fe−X[a]/Å	2.343	2.342	2.342	2.327
Fe−CO[a]/Å	1.790	1.792	1.792	1.798
Fe−CO_{axial}[a]/Å	1.821	1.824	1.824	1.816
X−X/Å	2.613	2.626	2.632	2.906
dihedral[b]	137.0	138.0	141.0	176.6
Fe−H[a]/Å	1.518	1.516	1.512	1.524
H−H/Å	2.066	4.311	4.334	3.104

[a] Average value. [b] Defined as the Fe−P−P−Fe dihedral angle.

Dihydrogen elimination from H_2**3P** might involve protonation of a basic terminally bound hydride or a dihydride such as down:down-H_2**3P**$_M$. The structures of H_2**DP** and H_2**FP** provide qualified support for the latter alternative. The striking difference in the rate of dihydrogen elimination from H_2**3P** and H_2**DP** might be reflected by the ground-state geometries, and the calculated structures of down:down-[H_2**3P**$_M$] and cis-[H_2**DP**$_M$] are shown in Figure 8. Clearly, the difference in the 2Fe2P core geometry has a significant effect on the H−H distance (Table 3). Computational studies of the reaction path for electrocatalytic proton reduction by **3S** have recently been reported.[42] The pathway is suggested

(41) Dobbie, R. C.; Whittaker, D. *J. Chem. Soc., Chem. Commun.* **1970**, 796−797.
(42) Greco, C.; Zampella, G.; Bertini, L.; Bruschi, M.; Fantucci, P.; Gioia, L. D. *Inorg. Chem.* **2007**, *46*, 108−116.

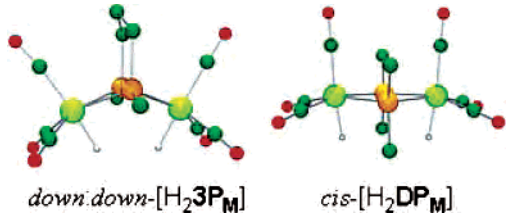

Figure 8. DFT-optimized geometries of selected protonated reduced forms of **3P** and **DP**; for clarity, non-hydride hydrogen atoms have been omitted.

to proceed through a bridging hydride, [H**3S**]$^-$, where protonation gives down:down-[H_2**3S**]. The transition state for dihydrogen elimination is calculated to have dihydrogen end-on-bound to one iron center and the second iron atom weakly interacting with the nonbound hydrogen atom.[42] The calculation of the structure of down:down-[H_2**3S**] was repeated so as to remove effects due to differences in basis set and indicated shorter Fe−Fe and H−H distances (Δr = 0.202 and 0.181 Å) than for down:down-[H_2**3P**$_M$]. The differences in calculated geometry for the respective doubly protonated, doubly reduced compounds, when taken together with the rates of dihydrogen elimination, provide strong support for the proposition that the electrocatalytic pathway for proton reduction at more moderate potentials (process 1) proceeds through a down:down dihydride such that the increase in rate is due to destabilization of the ground state and/or stabilization of the end-on-bound dihydrogen transition state by the closer proximity of the nonbound iron atom.

Conclusions

Linking the bridging phosphido groups of $Fe_2(\mu\text{-}PR_2)_2(CO)_6$ constrains the geometry of the 2Fe2P core, and this alters the relative energies of the reduced products. Although **3P**$^-$ is unstable with respect to disproportionation (K_{disp} = 13), a sufficient concentration can be obtained to allow IR and EPR characterization, together with an estimation of the Fe−Fe bond distance from EXAFS analysis.

The two-electron-reduced product has an IR spectrum closely related to that of the crystallographically characterized species **DP**$^{2-}$, and the long Fe−Fe contact of 3.55 Å confirms that the two electrons are added to an orbital of Fe−Fe antibonding character. DFT calculations of the redox series reproduce the structural parameters and IR spectra and suggest that **3P**$^{2-}$ has a distorted structure with a nonplanar 2Fe2P core geometry.

Even though **3P** displays an electrocatalytic response for proton reduction similar to that of **3S**, the paths leading to the respective two-proton, two-electron products are markedly different, and this is demonstrated most clearly by the one-electron (**3S**) and two-electron (**3P**) characters of the primary reduction. Formation of H_2**3S** proceeds by successive reduction and protonation steps[5] (ECEC reaction), whereas an EECC reaction provides a path to H_2**3P**. In the case of **3S**, the predominant mode for loss of the catalyst involves dimerization of **3S**$^-$, and this underlies CO inhibition of electrocatalysis. There appears to be no comparable dimerization products of **3P**$^-$, and there is no evidence for CO inhibition of electrocatalysis.

The absence of depletion/growth features during the initial phase of electrocatalytic proton reduction in thin-layer SEC experiments (Figure 7a) can only be interpreted in terms of a pathway for dihydrogen evolution from a two-electron-reduced form of **3P**. Electrochemical simulation of the voltammetry supports this conclusion (Figure 6). Provided that a core geometry similar to that of the dithiolato-bridged analogues can be obtained, dihydrogen evolution from the two-electron, two-proton form of the phosphido-bridged compound occurs at a comparable rate. A reaction path for dihydrogen evolution that involves protonation of a basic terminal hydrido ligand followed by oxidative elimination of dihydrogen would not be expected to have a high sensitivity to the 2Fe2X core geometry. The protonation chemistry of **DP**$^{2-}$ is well established with H**DP**$^-$ formed in reactions with weak acids for which the IR spectra show that a terminally bound hydride is formed,[25] an observation in keeping with DFT-based geometry optimization of H**3P**$^-$. Evidently, an Fe−Fe distance greater than 3.5 Å does not favor a bridged hydride. Reaction with stronger acids leads to formation of H_2**DP** without elimination of dihydrogen. Because the Fe−Fe distances are similar for the reduced forms of both compounds, the observation of proton reduction by **3P** and not **DP** would appear to rule out a reaction path mechanism centered on a single iron atom, such as protonation of a basic terminal hydrido ligand followed by oxidative elimination of dihydrogen.

DFT investigations of **3S** suggest a path for electrocatalytic proton reduction that involves a dihydride intermediate with hydride ligands bound to different iron atoms. Similar species were calculated for H_2**3P** and H_2**DP**, where, in each case, the productive isomer has the hydride ligands closest. The transition state has an end-on-bound dihydrogen ligand coordinated to one iron atom, with the nonbound iron and hydrogen atoms interacting weakly. The distortion of the core geometry by linking the bridging phosphido groups or by the presence of dithiolate bridging ligands reduces the H−H distance of the intermediate and gives a shorter nonbonded Fe−H distance for the transition state. Although the difference in electronic structure for S and P bridging ligands also makes a contribution, the relative rates of dihydrogen elimination from H_2**DP** (∼0), H_2**3P** (2.4), and H_2**3S** (4.0), together with the spectroscopic and SEC data and DFT calculations, are consistent with a reaction path that proceeds through an Fe_a:Fe_b dihydride. Clarification of the reaction path for bridged diiron compounds is important in terms of providing a blueprint for the refinement of systems of this sort for catalysis of proton reduction (and dihydrogen oxidation).

Acknowledgment. S.P.B. gratefully acknowledges the Australian Research Council for funding this research. M.H.C. gratefully acknowledges the University of Melbourne for the award of a scholarship, and S.J.B. acknowledges the

receipt of an Australian Postgraduate Research Award. The EXAFS experiments were performed at the Australian National Beamline Facility with support from the Australian Synchrotron Research Program, which is funded by the Commonwealth of Australia under the Major National Research Facilities Program. Mr. Mark I. Bondin and Dr. Garry Foran are thanked for expert assistance with the EXAFS experiments. Support from the Victorian Institute for Chemical Sciences High Performance Computing Facility is gratefully acknowledged. We thank Professor Luca De Gioia for providing a copy of his manuscript prior to publication.

Supporting Information Available: IR SEC results for **3P**; EPR spectra of $\mathbf{3P}^{-}$ (RT); fits of the EXAFS data of **3P**, $\mathbf{3P}^{2-}$, and a mixture of **3P**, $\mathbf{3P}^{-}$, and $\mathbf{3P}^{2-}$; summary of parameters used in the electrochemical simulation of electrocatalytic proton reduction by **3P**; final coordinates and calculated IR spectra for the DFT structure optimized species. This material is available free of charge via the Internet at http://pubs.acs.org.

IC0623361